



Experimental and numerical study of the mechanism of block–flexure toppling failure in rock slopes

Haina Zhang^{1,2} · Xinyang Xu¹ · Yun Zheng² · Huan Li^{2,3} · Haosen Guo¹

Received: 4 August 2021 / Accepted: 26 December 2021 / Published online: 10 January 2022
© Springer-Verlag GmbH Germany, part of Springer Nature 2022

Abstract

Block-flexure is the commonest mode of toppling failure and can be frequently encountered in anti-inclined rock slopes. In this work, the failure mechanism of block–flexure toppling (BFT) was investigated using centrifugal and numerical models. The numerical model was configured using the Universal Distinct Element Code (UDEC) and calibrated with the results of the centrifuge test. All the simulation results, including the measured displacements, failure load, and failure surface, are generally in line with that of experimental results. Further, the results of simulations show that, well before the appearance of instability in the jointed rock slope, slipping failure and opening fractures had occurred in the interlayer. Moreover, all the acting points of normal forces in steep joints are located between the bottoms and the midpoints of the columns under consideration, in the process of toppling failure. Finally, sensitivity of joint parameters, including the connectivity rate of discontinuous cross-joints, the thickness of the rock column joint, joint friction angle, and joint cohesion, were performed to investigate the effects of the tensile strength of intact rock. The results indicate that joint cohesion and thickness of the rock column greatly influence the failure load (represents safety factor of the slope). The connectivity rates of the discontinuous cross-joints and joint friction angle were found to have significant effects on the shape and location of the basal failure plane. This research would provide a deep understanding on the failure mechanism of BFT for relevant scholars.

Keywords Rock slope · Block–flexure toppling failure · Centrifuge model · Failure surface · UDEC

Introduction

Toppling rock slope is one of the most frequently occurring modes of instability in open-pit, hydropower, highway, and other engineering activities (Muller 1968; Wyllie 1980; Zhao et al. 2015; Gu and Huang 2016; He et al. 2018), and usually results in serious loss of life and property. Goodman and Bray (1976) originally divided the toppling failure into three main types: block toppling, flexural toppling, and block–flexure toppling (BFT). The block toppling and flexural toppling

deformation behavior and failure modes have been studied extensively by many scholars (e.g., Goodman and Bray 1976; Aydan et al. 1989; Adhikary et al. 1997; Liu et al. 2009; Liu and Zhao 2013; Chen et al. 2018; Zheng et al. 2019). BFT is characterized by block toppling of blocky columns and flexural toppling of continuous columns, as shown in Fig. 1a–b. However, no considerable attention has been paid to BFT as yet. Amini et al. (2012, 2015) proposed a theoretical model of BFT failure that was validated through tilting table experiments. However, their models in tilting table experiments are hardly to reproduce the stress states and failure behavior of real slopes due to dimensional effect. Centrifuge modeling is a powerful method of studying failure that occurs primarily because of bodily forces (Moo-Yong et al. 2003; Lin and Wang 2006; Hodder et al. 2010).

Numerical simulation can be capable of dealing with the complex geometry of the targeted area, providing a unique advantage to rapidly analyze the mechanism of toppling failure in rock slopes (Alejano et al. 2010; Mohammadi and Taiebat 2015; Yang et al. 2018; Zheng et al. 2021). For example, the Universal Distinct Element Code (UDEC), a commonly used

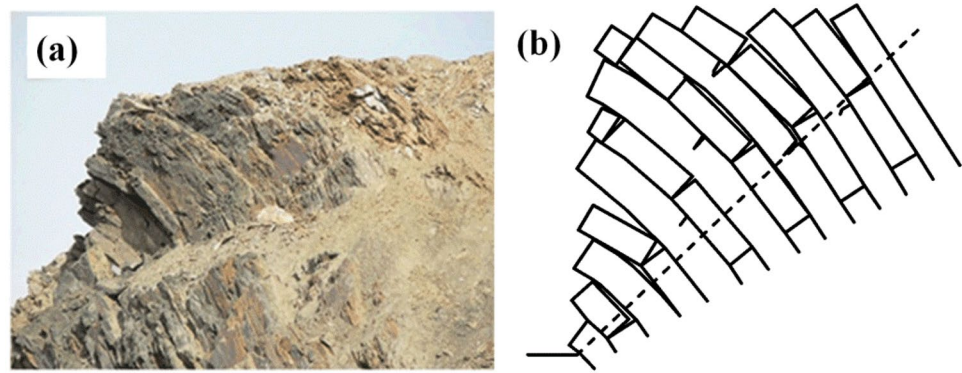
✉ Yun Zheng
yzheng@whrsm.ac.cn

¹ College of Civil Engineering and Architecture, East China Jiaotong University, Nanchang, Jiangxi Province 330013, China

² State Key Laboratory of Geomechanics and Geotechnical Engineering, Institute of Rock and Soil Mechanics, Chinese Academy of Sciences, Wuhan 430071, Hubei, China

³ Jiangxi Copper Technology Research Institute Co., Ltd. Nanchang, Jiangxi 330029, China

Fig. 1 Block–flexure toppling failure of a jointed rock slope: **a** in the field; **b** corresponding schematic diagram (modified from Goodman and Bray 1976)



simulation software for studying the instability mechanism of such failures, has ability to capture the rotation and sliding of blocks as well as the tensile or shear failure modes of intact block. Additionally, the validity of this method to simulate the toppling failure was initially verified by Barla et al. (1995). Alejano and Alonso (2005) calculated the safety factor of rock slopes against toppling failure using UDEC combined with the strength reduction method. Recently, Zheng et al. (2017, 2018) captured many aspects of flexural toppling using the strain-softening model of UDEC. Many other numerical methods have also been employed to study toppling failure in rock slopes, such as the finite element method, the continuum-based discrete element method, discontinuous deformation analysis, and the distinct lattice spring model (Adhikary and Dyskin 2007; Chen et al. 2015; Lian et al. 2017).

In this study, the failure mechanism of BFT was investigated through both centrifuge physical model tests and UDEC simulations. First, a physical model of jointed rock slope was prepared to pre-investigate the deformation and failure behavior of the slope. Then, the same model was configured in UDEC and the corresponding parameters of numerical models are calibrated by the results of the centrifuge experiment. The gravity increase method was employed in the UDEC simulation, which is similar to the loading process in the centrifuge experiment. Many mechanisms of BFT that cannot be revealed by a centrifuge experiment were discovered using the numerical model. Finally, influence factor analyses were carried out to investigate the effects of the tensile strength of intact rock, the connectivity rate of discontinuous cross-joints, the thickness of the rock column, joint friction angle, and joint cohesion on the BFT failure.

Centrifuge modeling

To study the failure mechanisms of BFT, a centrifuge test was performed with the TLJ-500 geotechnical centrifuge equipment at Changsha University of Science and Technology in China (Zhang et al. 2020), as shown in Fig. 2a. The real stress field in the slope prototype was simulated by applying a high centrifugal force field to the centrifuge model. Based on the law of similitude, the mechanical parameters of the physical model material (such as density, elastic modulus, and strength parameters) should be equal to that of the real rock (Zhang et al. 2007). The artificial material used in physical model consisted of gypsum powder, fine quartz sand, iron powder, and water in a ratio of 0.34:0.05:0.46:0.15 (by weight). Moreover, extensive rock mechanics tests were conducted to determine the specific mechanical properties of the material. The detailed results are listed in Table 1.

In reality, the failure process of a natural rock slope subjected to BFT failure is quite complicated. Based on the previous study (Amini et al. 2015), a simplified physical model was constructed to study the relevant failure mechanism in Fig. 2a (Zhang et al. 2020). Two groups of orthogonal joints pre-existed in the physical model. One group of joints dipped into the face of the slope with a steeply angle of 78° , forming continuous columns; while, the other was a group of pseudo-continuous cross-joints with connectivity rates of 0.5 cut alternate columns into blocks forming blocky columns. The slope was configured layer by layer using columns of these two types. To characterize the shear behavior of the weak interlayer more realistically, the sides of the columns

Fig. 2 Models of block–flexure toppling failure adopted in this study: **a** physical model (the local enlargement at the foot of the slope is shown); **b** numerical model with measured points (mm)

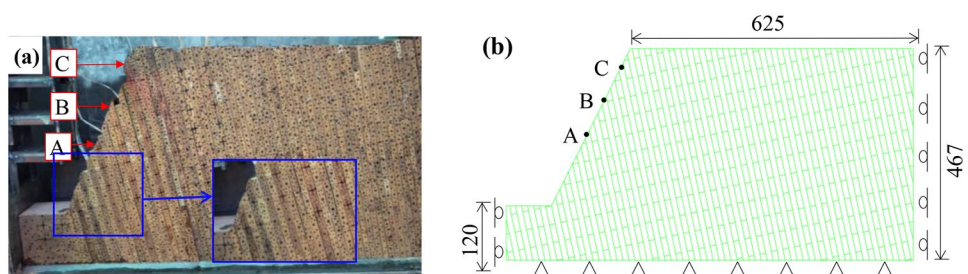


Table 1 The properties of the centrifuge model and calculation parameters used in the UDEC models

Model parameters	Value
Height of slope (mm)	347
Inclination of slope face (°)	63
Thickness of column (mm)	13
Height of blocks in blocky column (mm)	40
Inclination of cross-joint (°)	12
Unit weight (kN/m ³)	24.4
Uniaxial compression (MPa)	12.69
Modulus of elasticity (GPa)	2
Poisson's ratio	0.3
Tensile strength (MPa)	0.45–0.68 (0 [*])
Cohesive strength of artificial rock (MPa)	1.55 (0 [*])
Friction angle of artificial rock (°)	41 (41 [*])
Friction angle of interlayer (°)	18
Cohesion of interlayer (kPa)	1

* Residual values for friction, cohesion and tension of intact rock used in the strain-softening model of UDEC

were coated with Vaseline. The interlayer shear strength of the columns was determined by a joint shear test, as shown in Table 1. To record the deformation process of the slope, the horizontal displacements were monitored at three different points (A, B, C in Fig. 2a) at the surface using noncontact laser displacement meters.

The results show that as the g-level increased, so too did the displacements—slowly at first, and then much more rapidly (Fig. 5 in the “Verification with centrifuge experiment” section gives details). When the g-level reached 18.5 g, the slope underwent an instantaneous BFT failure with a stepped failure surface, as shown in Fig. 3a. Moreover, several significant V-shaped fractures can be captured clearly on the top of the slope. This behavior is a typical feature of toppling failure as noted by Wyllie and Mah (2004). A rotation of blocky columns was also observed, as seen in Fig. 3a. The rough fractures at the bottoms of continuous columns indicated the occurrence of tensile failure (Fig. 3b–d). Therefore, both blocky and flexural toppling—that is, BFT failure—occurred in the test (Goodman and Bray 1976). According to the deformation characteristics of the model, the failure zone can be carved into three subzones (Fig. 4): the toppling failure zone, which is delimited by the penetrating failure

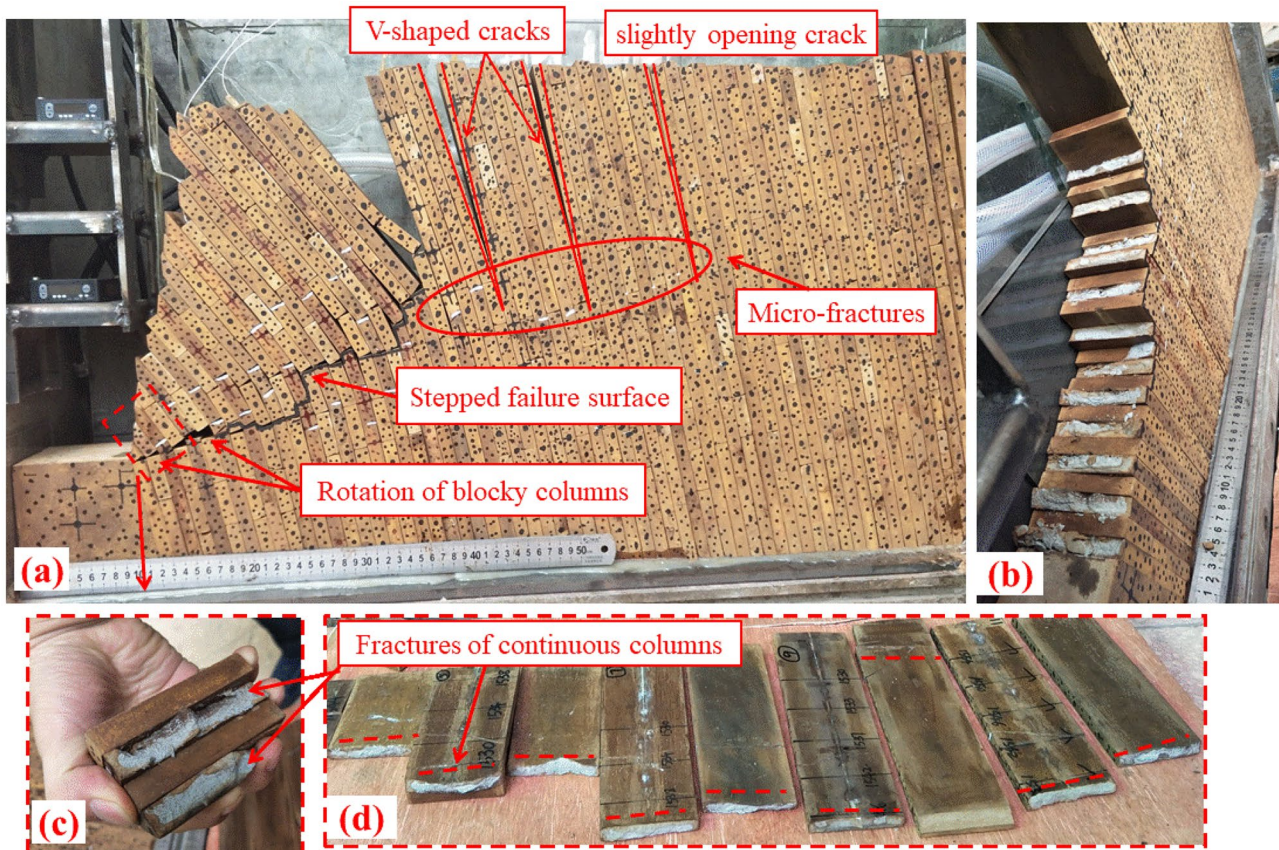
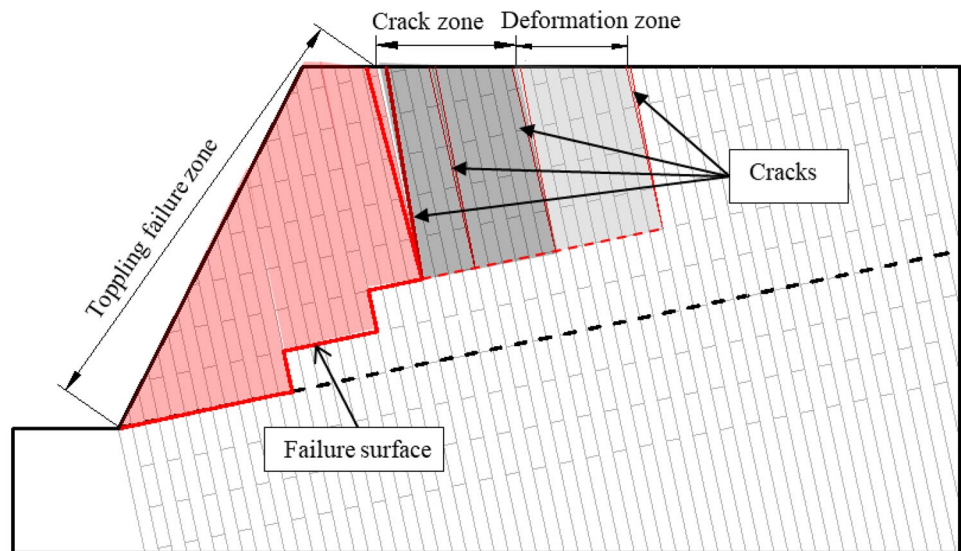


Fig. 3 Physical model, post-failure: (a) observed failure surface and cracks; (b) bottoms of toppling continuous and blocky columns; (c) bottoms of columns near toe of slope; (d) fractures of continuous columns

Fig. 4 Failure zones and failure surface of rock slope subjected to block–flexure toppling



surface; the crack zone, wherein V-shaped cracks form along the sides of columns; and the deformation zone, in which only a slight crack and micro-fractures can be observed on the sides of columns. The failure surface of the toppling failure zone can be seen clearly: it initializes at the toe of the slope and extends backward along the direction perpendicular to continuous joints, then steepens before the top of the slope with a block height (i.e., 40 mm). The failure surfaces of crack and deformation zones were found at the bottom of three V-shaped cracks, surrounded by micro-fractures (i.e., the white lines in Fig. 3a). The failure zones and failure surface of the post-failure model are presented in Fig. 4.

Configuration of numerical model

UDEC provides a prominent advantage for capturing the large deformation, failure behavior, and even failure process of discontinuous jointed rock masses with a relatively simple constitutive model and have been widely used in analysis of the toppling failures behavior (Alejano and Alonso 2005; Zheng et al. 2018). In the present study, to understand the failure mechanisms of rock slopes susceptible to BFT, a series of numerical simulations were carried out using UDEC.

In the numerical model, lateral boundaries were applied to roller conditions, and the bottom of the model was fixed (Fig. 2b). These boundary conditions are used widely. The geometries of the numerical model were identical as those of the experimental model. The model was divided into triangular zones with the maximum edge length of 6 mm. The strain-softening model was used to describe the mechanical behavior of intact rocks, while coulomb slip model was employed to simulate the slipping failures and opening fractures behavior of joints.

The calculation parameters of the numerical model are shown in Table 1. It should be noted that the normal and shear stiffness of joints used for the model cannot be determined from the artificial material. Fortunately, the normal stiffness (k_n) of the joints can be calculated by the following formula (Itasca 2011):

$$k_n = \max \left[\frac{K + \frac{4}{3}G}{\Delta Z_{\min}} \right] \quad (1)$$

where K is the bulk modulus, ΔZ_{\min} is the smallest width of an adjoining zone in the normal direction, and G is the shear modulus.

In principle, the value of k_n derived by Eq. (1) is within the range of 500 to 1500 GPa/m based on the variation of ΔZ_{\min} . Moreover, according to the research results of Zheng et al. (2018) and Alzoubi et al. (2010), the ratio of shear stiffness (k_s) to normal stiffness (k_n) was around 0.85. Thus, shear stiffness can be nailed down eventually through the aforementioned relationship. After that, the targeted values of k_n and k_s were verified based on the measured displacements in the experiment.

Simulation of block–flexure toppling failure

Verification with centrifuge experiment

The loading process of numerical simulation was consistent with that of the centrifuge test, whereby the gravity load increased gradually (the gravity increase method) with increments of 1 g. In each simulation, sufficient numerical time steps were set to ensure an equilibrium state in the model. Figure 5 shows the comparison between the displacements

of three points (A, B, C in Fig. 5) calculated by the UDEC and monitored by the centrifuge experiment, respectively. It is found that the simulated results are consistent with the measured data of the centrifuge experiment for the numerical cases of $k_n = 500$ GPa/m and $k_s = 425$ GPa/m. It can be observed that the displacement calculated by simulations increased steadily with slow rate in the early portion of the displacement–time curves, and then present a rapid increase with the g-level approached 18 g. Therefore, the failure load (18 g) obtained in the numerical simulation is also in agreement with that obtained in the centrifuge experiment (18.5 g).

The simulated results in Fig. 6 demonstrate that all the plasticity indicators of the zone state are tensile failure in continuous columns and that the tensile failure (represented by a pink circle) distributes in a stepped band. Interestingly, a similar failure band with a linear failure surface above and a basal plane below was also observed by Chen et al. (2015) during the research of block toppling failure, such that, the stepped basal plane (marked as a red line) was defined below the failure band to describe the depth and scope of the failure in this work. The results indicate that the failure scope obtained using the UDEC model is generally consistent with the three failure zones obtained from centrifuge.

Figure 7 shows the toppling model with addition of 5 million timesteps after the formation of the failure surface and its interlayer opening fractures. The opening fractures along the cross-joint show that the overturning of blocky columns also occurred. Thus, typical BFT failure can be reproduced by UDEC. Further comparison of experimental and numerical results shows that the UDEC model can provide a deeper understanding of the centrifuge results,

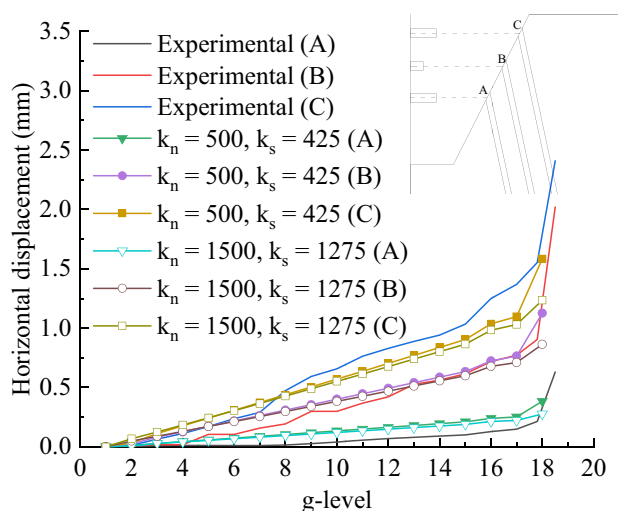


Fig. 5 Effects of normal and shear stiffness on deformation pattern ($\times 1$ GPa/m). Horizontal displacement at points A, B and C of numerical simulation and experimental results

and this demonstrates that it is feasible to use UDEC to study the failure mechanism of BFT.

Analysis of BFT failure process

Due to the limitations of measurement methods, many significant physical features, i.e., the evolution of inter-layer failure, particularly in the early phase, could not be discerned directly in the centrifuge test. However, these similar behavior characteristics formed in physical model test can be captured easily in the numerical model.

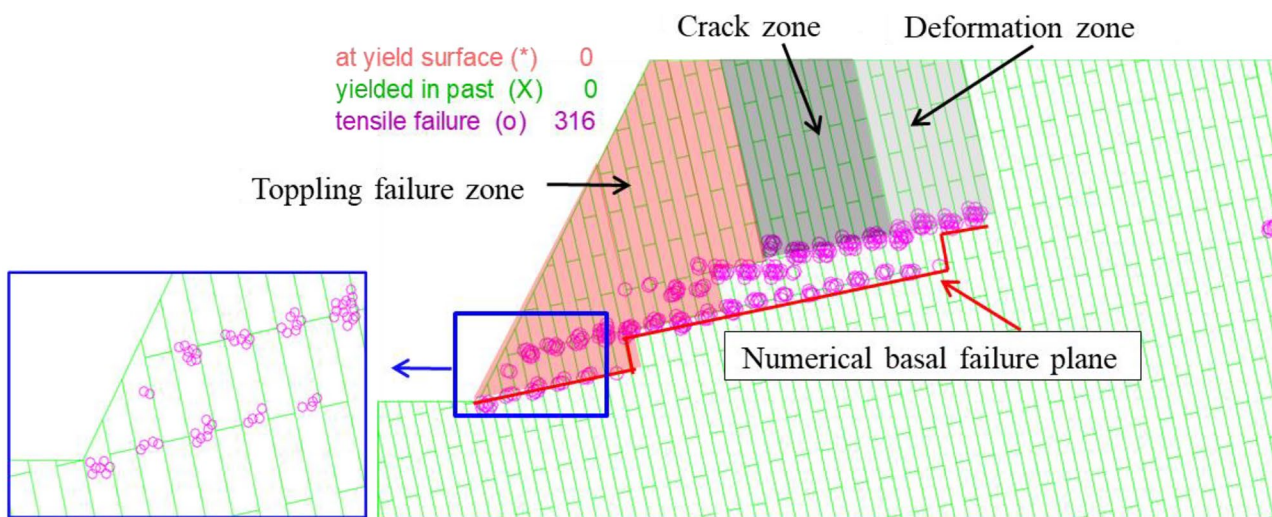


Fig. 6 Comparison of three failure zones of experimental results with the failure state obtained by numerical simulation. Also shown is the local enlargement at the foot of the slope

Fig. 7 Model with additional 5 million timesteps after formation of failure surface and interlayer opening fractures (in blue)

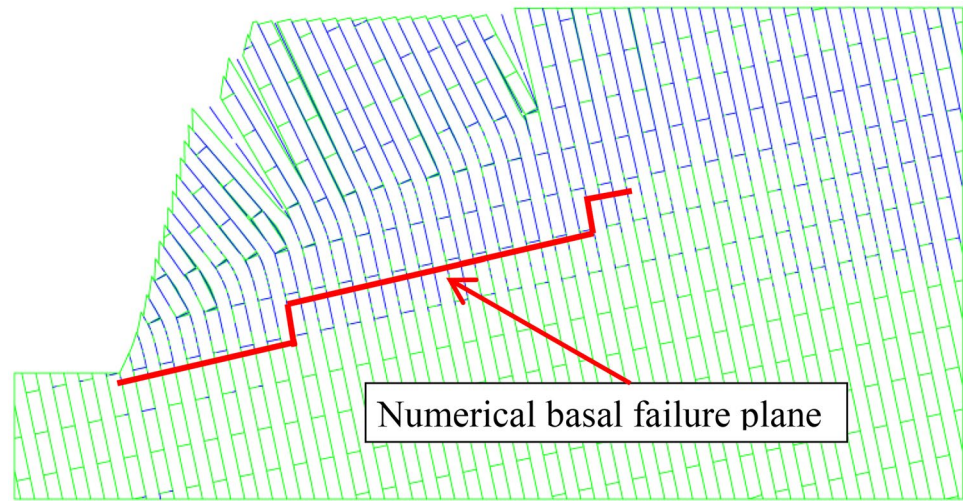


Figure 8 shows the distribution of interlayer opening fractures beneath different g -levels. It can be seen that the opening fractures (in blue) began to appear at the back of the slope at 2 g . As the g -level approached 5 g , the failure scope of the interlayer opening nearly reached the maximum, and with the further increase in acceleration, the interlayer failure scope did not develop any further. This indicates that the overturning mainly occurred in the early stage of loading. Moreover, major of ultimate interlayer opening fractures only occurred above the basal plane, along the set of joints dipping into the slope face; some also occurred along cross-joints near the basal failure plane.

Figure 9 presents the distribution of interlayer slipping failure at different g -levels. A difference for interlayer slipping failure (shown in red in Fig. 9) along the set of joints dipping into slope face was that it began from the bottom of the slope and then gradually developed to the rear edge of slope top. As for interlayer opening fractures, as the g -level approached 5 g , the failure scope of slipping failure reached

its maximum, and the failure did not develop further with the increase in acceleration. The ultimate slipping depth of the interlayer is deeper than that of basal failure plane.

Zheng et al. (2018) divided the deformation process of flexural toppling failure into three stages: elastic deformation due to cohesion, development of flexural toppling failure, and formation of the total failure surface. The authors found that these designations were largely suitable for BFT failure; due to the low cohesion of the joints, the elastic deformation stage was excluded. Therefore, according to the deformation pattern (Fig. 5) and the process of interlayer failure (Figs. 8, 9), there are two stages of BFT failure: development of flexural toppling failure (1–17 g , including interlayer failure) and formation of the total failure surface (17–18 g). Compared with the centrifuge test results, the numerical modeling results provide deep insights into the failure characteristics of block–flexure toppling.

The point at which the side force acts on the column is the most important parameter in the theoretical analysis

Fig. 8 Distribution of the interlayer opening fractures: **a** g -level = 2 g ; **b** g -level = 5 g ; **c** g -level = 15 g ; **d** g -level = 18 g

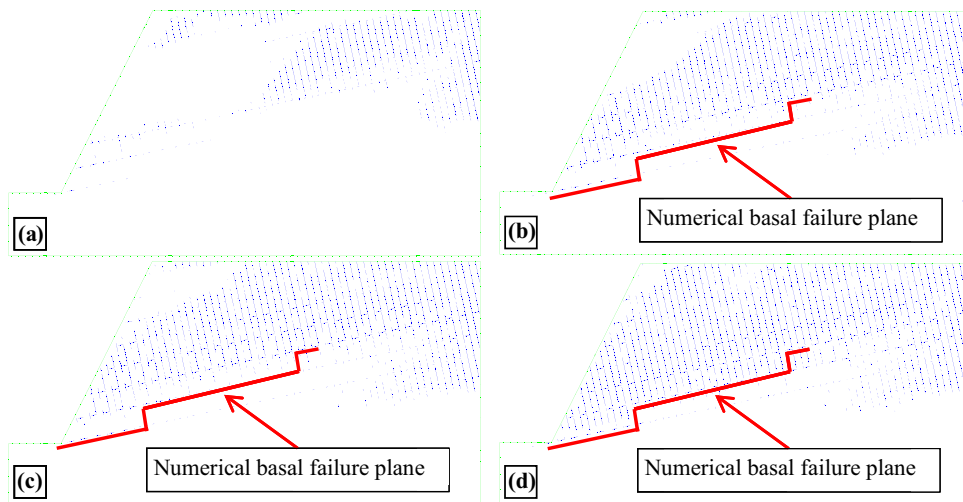
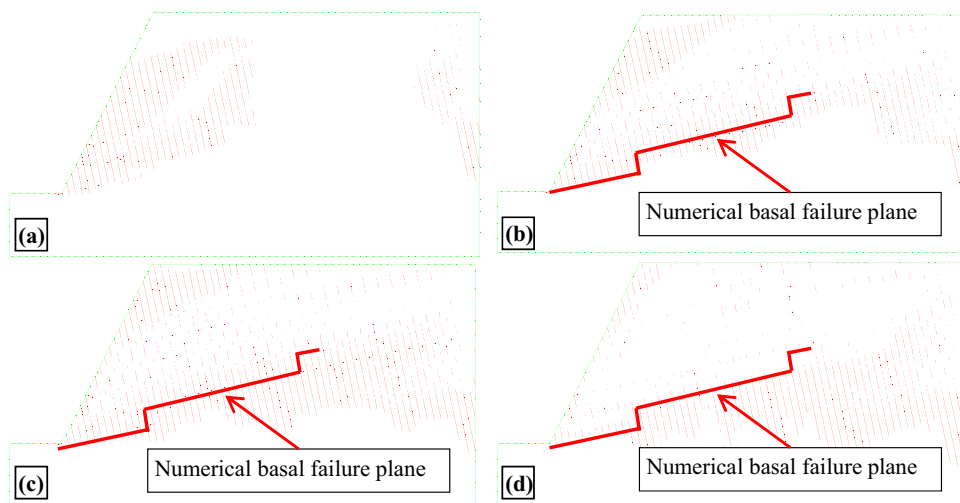


Fig. 9 Distribution of the interlayer slipping failure: **a** g-level=2 g; **b** g-level=5 g; **c** g-level=15 g; **d** g-level=18 g



of toppling failure; however, it is difficult to measure this directly using the physical model. Fortunately, it could be obtained easily in the numerical simulation using UDEC combined with developed fish functions. Zheng et al. (2018) used the dimensionless parameters λ and χ to study the total normal force and acting point of normal forces in steep joints. The dimensionless parameters of normal force in a steep joint (λ) is defined as follows:

$$\lambda = \frac{P}{n\gamma Hb} \tag{2}$$

where P is the total normal-contact forces above the basal failure plane, n is the g-level, and γ is the unit weight of the rock mass. H and b are the slope height and the thickness of columns, respectively.

The acting point of normal forces in steep joints (χ) is determined as follows:

$$\chi = \frac{\sum_{j=1}^m P_j x_j}{h \sum_{j=1}^m P_j} \tag{3}$$

where P_j is the normal force of interlayer contact j , m is the sum of interlayer contacts at a joint above the basal failure plane, x_j is the distance from contact j to the basal plane, and h is the height of the column above the basal failure plane.

In this study, Fish functions were used to extract the magnitude and action point of normal forces in steep joints above the basal failure plane, and the results are presented in Figs. 10

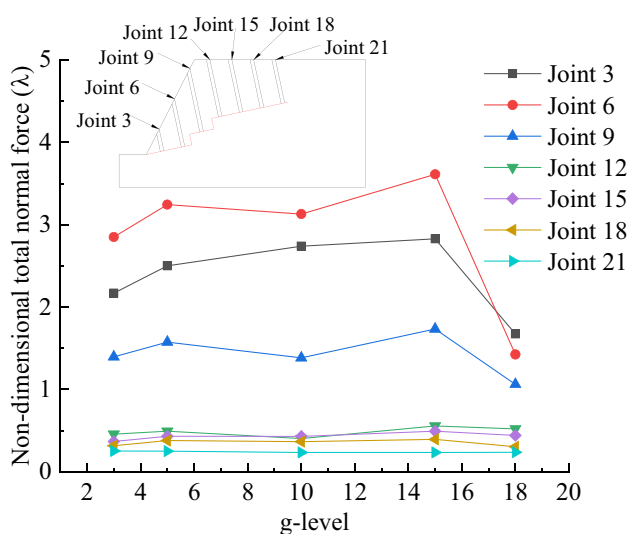


Fig. 10 Inter-column normal forces in different failure zones during toppling failure

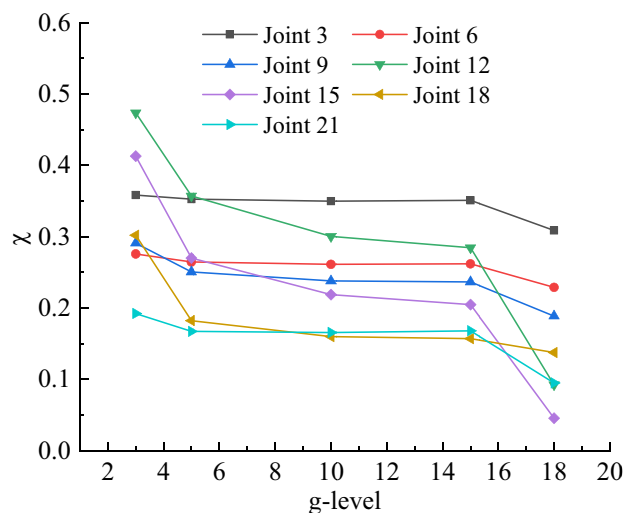
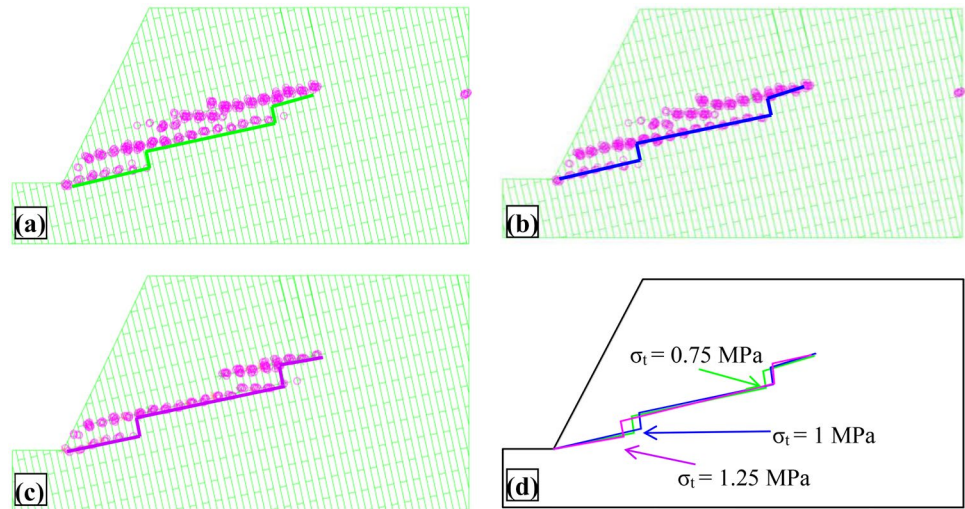


Fig. 11 Acting points of total normal forces in steep joints in different failure zones during toppling failure

Fig. 12 Basal failure planes of jointed rock slope under different tensile strengths of intact rock: **a** $\sigma_t = 0.75$ MPa; **b** $\sigma_t = 1$ MPa; **c** $\sigma_t = 1.25$ MPa; **d** comparison



and 11, respectively. It can be seen from Fig. 10 that the normal forces in steep joints below the slope surface were far greater than those below the top of the slope. This is due to the transfer of force from the back of slope to the foot of slope in the process of toppling deformation. Moreover, with the increase in g -level, λ did not change significantly at first. However, when the basal failure plane formed (i.e., the g -level approached 18 g)—which means that the energy has been released and stress concentration alleviated—the λ below the slope face decreased.

As shown in Fig. 11, with the increase of g -level, the value of χ decreased totally; that is, the acting points were closer to the bottom of the columns. Liu et al. (2009) proposed that the bottom of a block will be subjected to greater constraints as toppling failure occurs. In this model—because of the existence of alternate blocky columns—as toppling failure occurred, the normal forces at the bottom of the columns would have been greater, due to bottom constraints. Moreover, during the process of BFT failure, all the acting points of normal forces in steep joints are located between the bottoms and midpoints of the columns under consideration; that is, the value of x ranges from 0 to 0.5.

Influence factor analyses

According to the above analyses of a model employing centrifuge modeling and the numerical method, many factors notably influence the failure mechanism of block–flexure toppling, such as tensile strength of intact rock, connectivity rate of discontinuous cross-joints, joint friction angle, joint cohesion, and the thickness of the rock column. In this section, numerical models with different values of these parameters were analyzed in relation to basal failure plane, deformation mode, and failure load.

Tensile strength of intact rock

Figure 12 shows stepped basal failure planes under different tensile strengths (marked by green, blue, and purple lines). It can be seen that many columns underwent tensile failure and formed basal failure planes and that the columns performed similarly under different tensile strengths. This indicates that the tensile strength of intact rock has no obvious association with the location and shape of basal failure planes.

Fig. 13 Failure load and deformation under different tensile strengths of intact rock: **a** relationship between failure load and tensile strength of intact rock; **b** horizontal displacement at three measured points

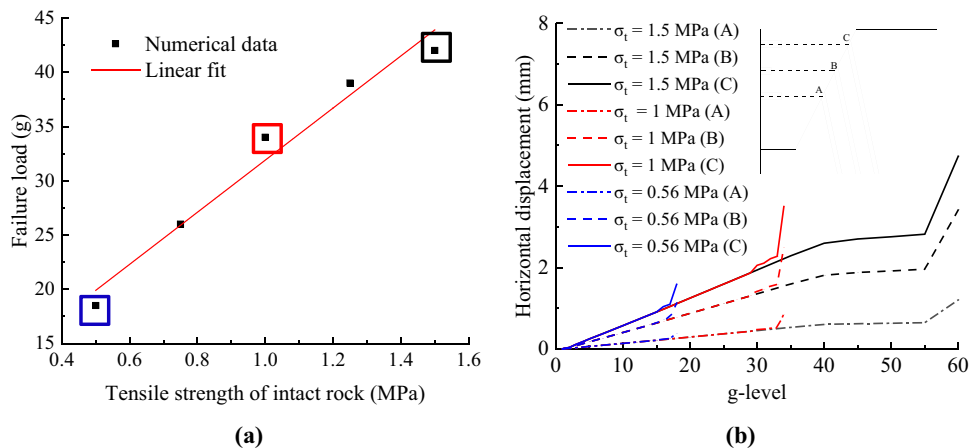


Figure 13a indicates that failure loads increase linearly with increases in tensile strength. During the loading process, the horizontal displacement of three points, A, B, and C, were recorded and their displacement values were extracted at tensile strengths of 0.5, 1, and 1.5 MPa, respectively. The failure loads of the three different tensile strengths are marked by boxes in Fig. 13a; the color of a box is the same as that of the displacement curve as shown in Fig. 13b. The results show that, prior to the occurrence of instability, the horizontal displacement values of slopes under different tensile strengths are exactly the same. This indicates that, in the early stage, toppling deformation is not affected by tensile strength. However, when failure loads are reached, the displacement of measured points increases sharply, and instability of the slope then occurs. Therefore, the tensile strength of intact rock can greatly affect the stability of rock slopes prone to BFT, but has an insignificant effect on the basal failure plane and the deformation mode.

Connectivity rates of discontinuous cross-joints

Connectivity rate (C_r) is an index of joint development, as shown in Fig. 14. The connectivity rate is defined as $C_r = m / (m + n)$, where m is the length of the discontinuous joint and n the length of the rock bridge. The greater the connectivity rate of cross-joints, the more fragmented the rock mass.

Figure 15 shows the simulated results of basal failure planes under cross-joints with different connectivity rates. It is clear that all the plasticity indicators showed

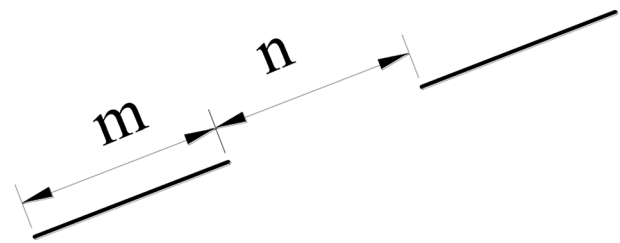


Fig. 14 Discontinuous joints in rock mass

tensile failure due to toppling deformation. The model in Fig. 15a suffered from flexural toppling failure, and the basal failure plane was relatively smooth because it was not affected by discontinuous joints. With an increase in the connectivity rate of discontinuous joints, the length of the stepped basal failure plane from the toe of slope also tends to increase. Due to the shear and tensile strengths of discontinuous joints being very low, the block can transfer the force to the continuous column through its rotation and slip, which results in stress concentration in the continuous column near the discontinuous joints. Therefore, the discontinuous cross-joints affect the shape of the basal failure plane.

Figure 16a shows that the failure loads of the slope decreased linearly with increases in the connectivity rates of discontinuous joints, which means that the stability of the jointed slope became worse. During the loading process, the authors extracted horizontal displacement values from the models at connectivity rates of 0, 0.25, and 0.5. The results (see Fig. 16b) show that the effects of the connectivity rate of discontinuous joints on the slope deformation mode are not significant.

Fig. 15 Basal failure planes of models under cross-joints with different connectivity rates C_r : a ideal anti-inclined slope without cross-joints ($C_r=0$); b $C_r=0.25$; c $C_r=0.5$; d comparison

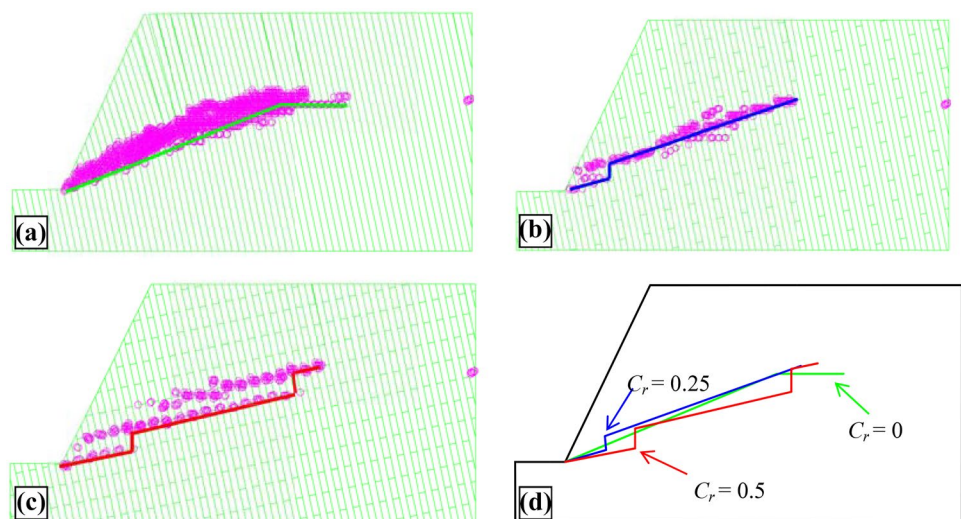
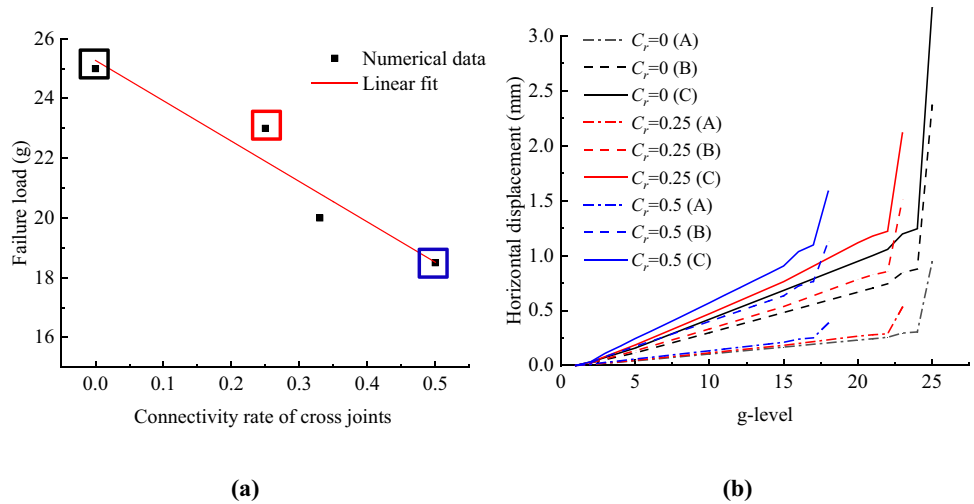


Fig. 16 Failure load and deformation under different connectivity rates: **a** relationship between failure load and connectivity rate; **b** horizontal displacement at three measured points



Joint friction angle

The results in Fig. 17 show that many columns undergo tensile failure forming basal failure planes. It can be seen that the location of the stepped basal failure plane becomes shallow with the increase of friction angle of joints. For example, when $\varphi_j = 13^\circ$, the basal failure plane extends upward along the cross-joints starting from the toe of the slope, while when $\varphi_j = 33^\circ$, the basal failure plane extends upward along the cross-joints above the toe of the slope. This is because the increase of joints makes it harder for deep interlayer slipping to emerge. Moreover, interlayer slipping is a prerequisite for toppling failure. Therefore, joint friction angle has a significant influence on the location and shape of the basal failure plane.

Figure 18a shows that there was an almost linear relationship between the friction angle of joints and the failure load of the jointed slope, which indicates that the increase of the joint friction angle can increase the stability of the slope.

Figure 18b presents displacement results at the joint friction angles of $\varphi_j = 13^\circ$, $\varphi_j = 23^\circ$, and $\varphi_j = 33^\circ$. It shows that, at the same g-level, slope deformation was reduced greatly by an increase in the friction angle. Therefore, grouting concrete into the rock joints, an efficient way to increase joint friction angle, can prevent large deformation of such slopes, as noted by Lian et al. (2017).

Joint cohesion

Figure 19 shows the stepped basal failure planes of jointed slopes under different joint cohesions. The results in Fig. 19d show that the stepped basal failure plane extended further with increases in joint cohesion. The reason for this is that when joint cohesion increases, the interlayer slipping failure becomes harder and so requires a larger load for toppling failure to occur. In addition, the larger failure load reduces the critical fracture height (h_{cr}) of an inclined column in the

Fig. 17 Basal failure planes of jointed rock slope under different joint friction angles: **a** $\varphi_j = 13^\circ$; **b** $\varphi_j = 23^\circ$; **c** $\varphi_j = 33^\circ$; **d** comparison

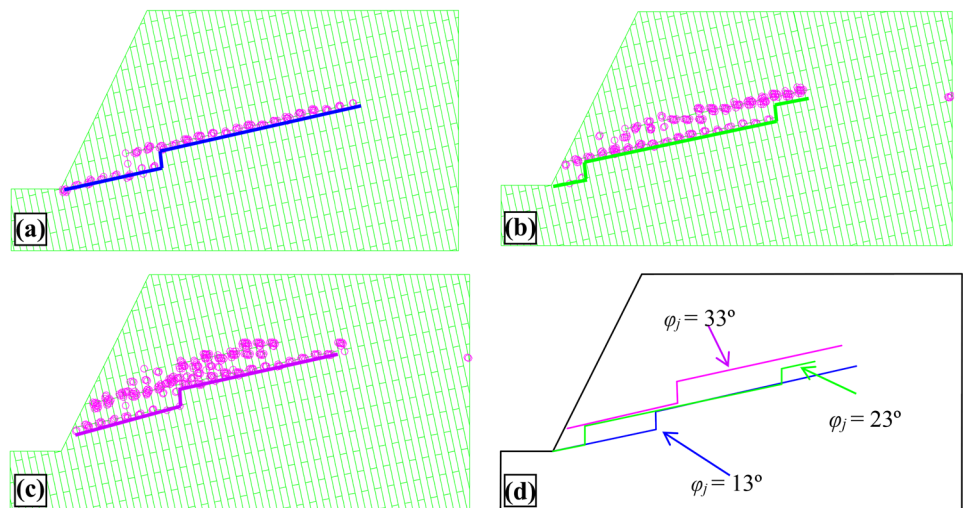
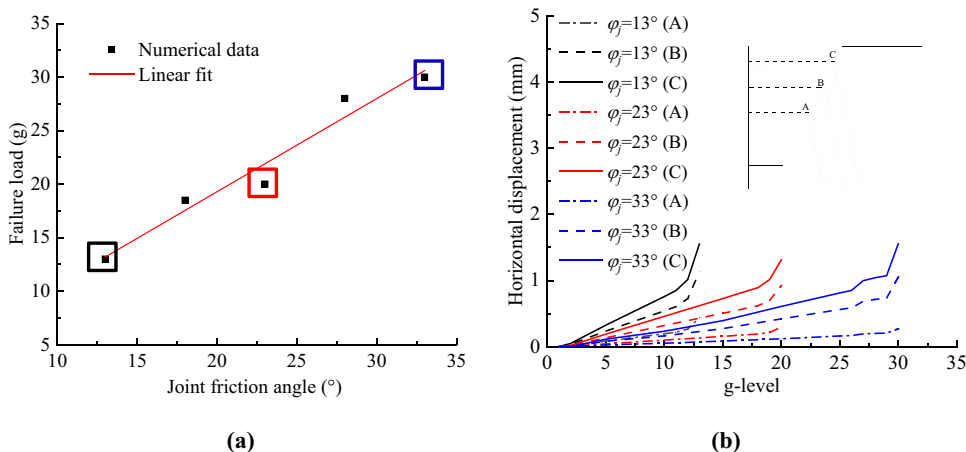


Fig. 18 Failure load and deformation under different joint friction angles: **a** relationship between failure load and joint friction angle; **b** horizontal displacement at three measured points



deformation zone shown in Fig. 19a. The critical fracture height can be obtained by the following equation (Aydan and Kawamoto 1992):

$$h_{cr} = \frac{b \cos \beta + \sqrt{b^2 \cos^2 \beta + 12 b \sin \beta \sigma_t / n \gamma}}{6 \sin \beta} \quad (4)$$

where b is the thickness of the column, β is the angle from the cross-joint to the horizontal line, and σ_t is the tensile strength of the continuous column.

The influence of joint cohesion on the basal failure plane could be observed owing to the sufficient boundary conditions of the model. By contrast, Alzoubi et al. (2010) proposed that joint cohesion had no influence on the basal failure plane of the slope because of the limited boundary conditions of the model.

Figure 20a shows that failure load increased nearly quadratically (i.e., steeply) with increased joint cohesion. Figure 20b shows the curves of horizontal displacement with

different g -levels at different joint cohesions. The results show that with an increase in g -level, there was a stage of elastic deformation due to cohesion at the beginning of the loading process. As the acceleration increased to a certain value (at which interlayer slipping failure begins to occur), the displacements increase gradually as a result of the development of toppling failure. Finally, when the acceleration reaches the failure load (i.e., the basal failure plane is formed), the displacements of measured points increase suddenly. As shown in Fig. 20b—take $C_j^\circ = 5$ kPa as an example—the deformation process is divided into three stages. Moreover, with increases in joint cohesion, the stage of elastic deformation increases significantly.

Wyllie et al. (2004) proposed the mechanisms of flexural toppling failure that the interlayer slipping failure and bending deformation will occur first, and that the failure surface will then begin to form. In the deformation process, joint cohesion controls the initiation of interlayer slipping failure.

Fig. 19 Basal failure planes of jointed rock slope under different joint cohesions: **a** $C_j = 1$ kPa; **b** $C_j = 10$ kPa; **c** $C_j = 15$ kPa; **d** comparison

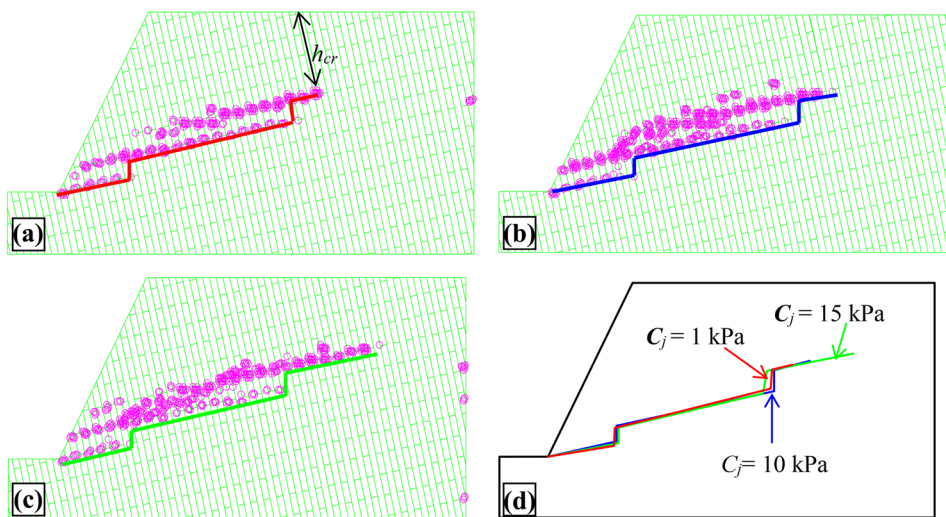
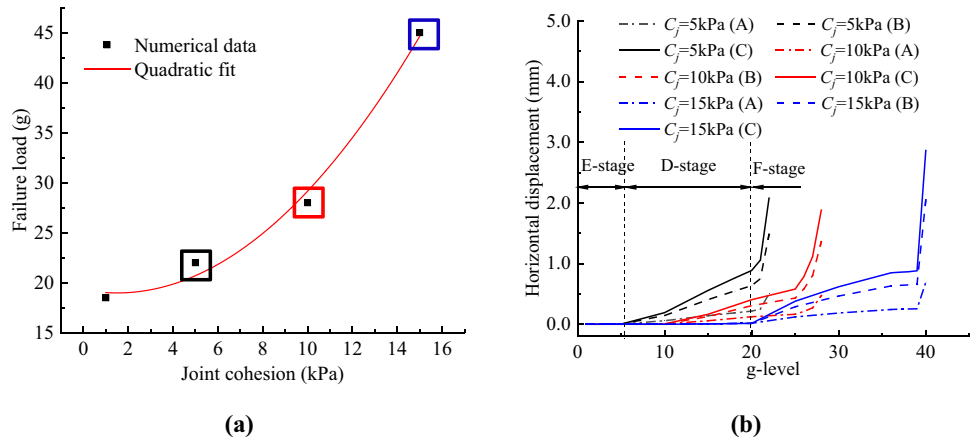


Fig. 20 Failure load and deformation under different joint cohesions: **a** relationship between failure load and joint cohesions, **b** horizontal displacement at three measured points. E-stage, D-stage and F-stage refer to the stage of elastic deformation, development of toppling deformation and formation of the basal failure plane



When joint cohesion is small, interlayer slipping failure will occur under the small g-level, while when joint cohesion is large, the deformation of toppling failure can be resisted.

The thickness of the rock column

As shown in Fig. 21, the basal failure planes of jointed slopes are formed under different thicknesses of the rock column by tensile failure due to low tensile strength. It can be seen from the comparison in Fig. 21d that the thickness of the rock column had only a minor influence on basal failure planes.

Figure 22a plots that failure load increased quadratically (i.e., steeply) with increased thickness of the rock column. For a cantilevered continuous column, the maximum tensile stress at the basal plane can be computed as follows (Aydan and Kawamoto 1992):

$$\sigma_t^{\max} = \frac{0.5M \cdot b}{I} - \frac{N}{b} = \frac{6M}{b^2} - \frac{N}{b} \tag{5}$$

where $I = b^3/12$, M is the bending moment at the base of the continuous column, $N \cong w \sin \theta$, w is the weight of continuous column above the basal plane, and θ is the dip angle of the continuous column.

It can be seen from Eq. (5) that when the thickness of the column increased, the tensile stress in the column tended to decrease, and thus it was harder to reach the tensile strength of the column. For the blocky columns, the corresponding slenderness ratios (defined as the ratio of the height of the blocky column above the failure surface to block thickness; Liu et al. 2009) decreased with increases in block thicknesses, which implies that toppling failure was less likely to occur. Therefore, the thickness of the rock column has a significant influence on the stability of jointed slopes subjected to BFT failure. Figure 22b shows that in the deformation process, with increases in the thickness of the rock column, the displacements of measured points decreased significantly due to it being more difficult for the toppling deformation to occur.

Fig. 21 Basal failure planes of jointed rock slope under different thicknesses of rock column: **a** $b = 13$ mm; **b** $b = 19.5$ mm; **c** $b = 32.5$ mm; **d** comparison. It should be noted that the case of the equal thickness of columns in one model is only considered

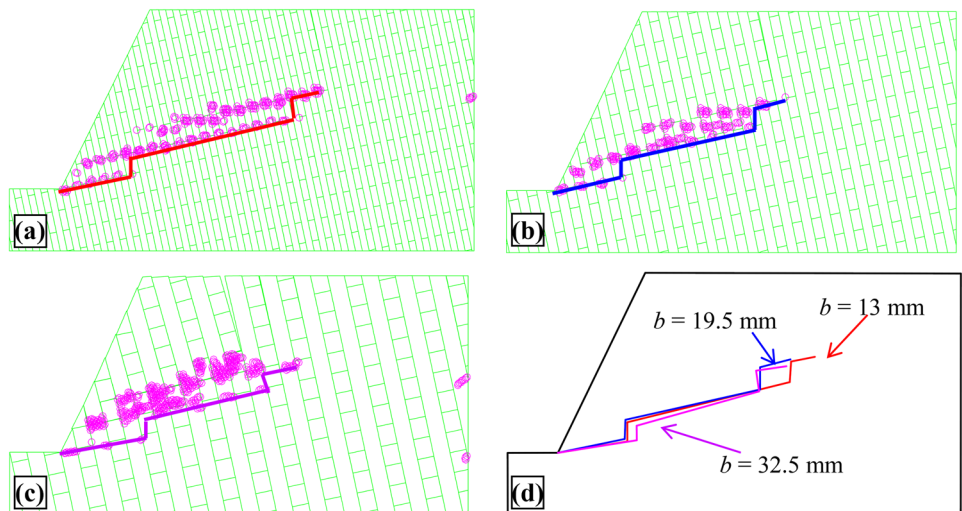
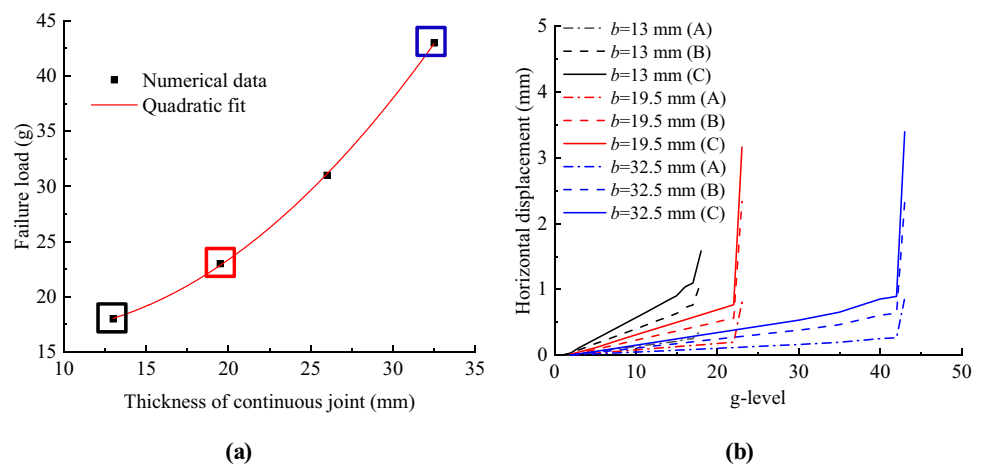


Fig. 22 Failure load and deformation under different thicknesses of rock column: **a** relationship between failure load and thickness of rock column; **b** horizontal displacement at three measured points

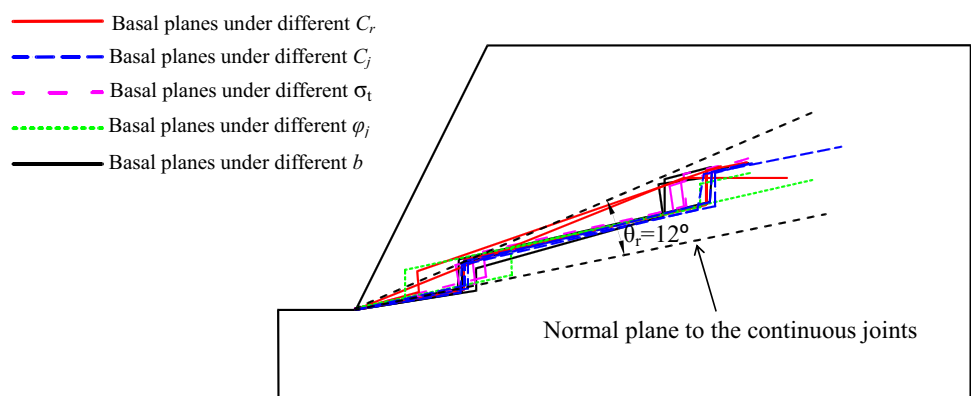


Discussion

To date, several scholars have conducted studies on the position and shape of the failure surface in flexural toppling failure. Employing a method of stability analysis based on limit equilibrium theory, Aydan and Kawamoto (1992) proposed the assumption that the failure surface is perpendicular to the discontinuities. Adhikary et al. (1997) further studied flexural toppling failure using centrifuge models and found that the failure surface started from the toe of the slope and was oriented at an angle of 12–20° upward from the normal to the failure surface (the angle is defined as θ_r). More recently, Zheng et al. (2018) proposed that failure surfaces should be investigated using an accurate searching method. He found that the failure surface is usually multi-planar, a result is similar to those observed in the centrifuge experiment and simulations in this paper.

This study has investigated the location and shape of basal failure planes of BFT failure under different influence factors. The basal failure planes of numerical models under different influence factors are summarized in Fig. 23. It can be seen that the stepped basal failure planes are within 12° upward from the normal plane of the continuous joints. It should be noted that basal failure planes can be computed by analyzing the stability of every block and every incorporation of contiguous blocks against sliding and toppling based on limit equilibrium method. Accordingly, the basal planes of instability of incorporation (block, clusters of blocks or the whole column) form the failure planes. Thus, the basal failure planes determined in this work is rigorous theoretically. However, scanning all the possible combinations is very low-efficient and time-consuming. Stochastic optimization method, such as genetic algorithm or particle swarm method may provide an excellent choice to solve this problem (Zheng et al. 2020a, b).

Fig. 23 Summary of basal failure planes under different influence factors: tensile strengths of intact rock (σ_t); connectivity rates (C_r); joint cohesions (C_j); joint friction angles (φ_j); thicknesses of rock column (b)



Conclusions

In this work, the failure mechanism of block–flexure toppling (BFT) of rock slopes was studied using the centrifuge and numerical (UDEC) models. The results of centrifuge experiments and numerical analyses are summarized as follows:

(1) The experiments show that BFT failure of the slope model occurs instantaneously with a stepped failure surface. The failure zone can be divided into three subzones: the toppling failure zone, the crack zone, and the deformation zone.

(2) UDEC is well suited to simulating BFT failure in rock slopes. Many aspects of such failures can be revealed by the UDEC model, combined with the strain-softening and coulomb slip models for intact rock and joints, respectively.

(3) Interlayer slipping failures and opening fractures occur far before BFT failure, especially along the group of joints dipping into the slope face. Moreover, in the process of toppling failure, all the acting points of normal forces in steep joints are located between the bottoms and the mid-points of the columns under consideration; that is, the value of x ranges from 0 to 0.5.

(4) The failure load increases linearly with increases in tensile strength and joint friction angle with keeping the other parameters constant, while failure load decreases linearly as the connectivity rate of discontinuous cross-joints increases. Additionally, the failure load increases nearly quadratically with augment of joint cohesion and thickness of the rock column.

(5) The connectivity rates of the discontinuous cross-joints and joint friction angle greatly influence the shape and location of the basal failure plane, while those of the tensile strength of intact rock, joint cohesion, and the thickness of the rock column are less significant.

Funding This research was financially supported by the National Natural Science Foundation of China (Grant Nos. 12072358 and 11472293), the Science and Technology Research Project of Education Department of Jiangxi Province (Grant No. GJJ200661) and the Natural Science Foundation of Jiangxi, China (Grant No. 20202BABL214051), the Open Research Fund of State Key Laboratory of Geomechanics and Geotechnical Engineering, Institute of Rock and Soil Mechanics, Chinese Academy of Sciences (Grant NO. Z020021).

References

- Adhikary DP, Dyskin AV, Jewell RJ, Stewart DP (1997) A study of the mechanism of flexural toppling failure of rock slopes. *Rock Mech Rock Eng* 30(2):75–93
- Adhikary DP, Dyskin AV (2007) Modelling of progressive and instantaneous failures of foliated rock slopes. *Rock Mech Rock Eng* 40(4):349–362
- Alejano LR, Alonso E (2005) Application of the shear and tensile strength reduction technique to obtain factors of safety of toppling and footwall rock slopes. *Impact of Human Act Geol Environ* 7–13
- Alejano LR, Iván GM, Roberto MA (2010) Analysis of a complex toppling-circular slope failure. *Eng Geo* 114(1):93–104
- Alzo'ubi AK, Martin CD, Crudden DM (2010) Influence of tensile strength on toppling failure in centrifuge tests. *Int J Rock Mech Min* 47(6):974–982
- Amini M, Gholamzadeh M, Khosravi H (2015) Physical and theoretical modeling of rock slopes against block-flexure toppling failure. *Int J Min Geol Eng* 49:155–171
- Amini M, Majidi A, Veshadi MA (2012) Stability analysis of rock slopes against block-flexure toppling failure. *Rock Mech Rock Eng* 45(4):519–532
- Aydan Ö, Kawamoto T (1992) The stability of slopes and underground openings against flexural toppling and their stabilisation. *Rock Mech Rock Eng* 25(3):143–165
- Aydan Ö, Shimizu Y, Ichikawa Y (1989) The effective failure modes and stability of slopes in rock mass with two discontinuity sets. *Rock Mech Rock Eng* 22(3):163–188
- Barla G, Borri-Brunetto M, Devin P, Zaninetti A (1995) Validation of a distinct element model for toppling rock slopes. 8th ISRM Congress. International Society for Rock Mechanics and Rock Engineering, Tokyo, Japan, pp 417–421
- Chen GQ, Chen T, Chen Y, Huang R, Liu M (2018) A new method of predicting the prestress variations in anchored cables with excavation unloading destruction. *Eng Geo* 241:109–120
- Chen ZY, Gong WJ, Ma GW, Wang J, He L, Xing YC, Xing JY (2015) Comparisons between centrifuge and numerical modeling results for slope toppling failure. *Sci China Technol Sc* 58(9):1497–1508
- Goodman RE, Bray JW (1976) Toppling of Rock Slopes. Proc., ASCE, Specialty Conf. on Rock Engineering for Foundations and Slopes. ASCE, Boulder Colorado 201–234
- Gu DM, Huang D (2016) A complex rock topple-rock slide failure of an anaclinal rock slope in the Wu Gorge, Yangtze River, China. *Eng Geo* 208:165–180
- He L, Tian Q, Zhao ZY, Zhao XB, Zhang QB, Zhao J (2018) Rock slope stability and stabilization analysis using the coupled DDA and FEM method: NDDA Approach. *Int J Geomech* 18(6):04018044
- Hodder MS, White DJ, Cassidy MJ (2010) Analysis of soil strength degradation during episodes of cyclic loading, illustrated by the T-Bar penetration test. *Int J Geomech* 10(10):117–123
- Itasca Consulting Group Inc (2011) UDEC (universal distinct element code), Version 4.0, Minneapolis
- Lian JJ, Li Q, Deng XF, Zhao GF, Chen ZY (2017) A numerical study on toppling failure of a jointed rock slope by using the Distinct Lattice Spring model. *Rock Mech Rock Eng* 3:1–18
- Lin ML, Wang KL (2006) Seismic slope behavior in a large-scale shaking table model test. *Eng Geo* 86(2):118–133
- Liu CH, Jaksa MB, Meyers AG (2009) A transfer coefficient method for rock slope toppling (EI). *Can Geotech J* 46(1):1–9
- Liu F, Zhao J (2013) Limit analysis of slope stability by rigid finite element method and linear programming considering rotational failure. *Int J Geomech* 13(6):827–839
- Mohammadi S, Taiebat H (2015) H-adaptive updated Lagrangian approach for large-deformation analysis of slope failure. *Int J Geomech* 15(6):04014092
- Moo-Yong H, Myers T, Tardy B, Ledbetter R, Vanadit-Ellis W (2003) Centrifuge simulation of the consolidation characteristics of capped marine sediment beds. *Eng Geo* 70(3):249–258
- Muller L (1968) New considerations on the Vaiont slide. *Rock Mech Eng Geo* 6(1):1–91
- Wyllie DC (1980) Toppling rock slope failures examples of analysis and stabilization. *Rock Mech* 13(2):89–98
- Wyllie DC, Mah C (2004) *Rock slope engineering*, Fourth Edition, 4th edn. Spon Press, London

- Yang YT, Xu DD, Zheng H (2018) Explicit discontinuous deformation analysis method with lumped mass matrix for highly discrete block system. *Int J Geomech* 18(9):04018098
- Zhang JH, Chen ZY, Wang XG (2007) Centrifuge modeling of rock slopes susceptible to block toppling. *Rock Mech Rock Eng* 40(4):363–382. <https://doi.org/10.1007/s00603-006-0112-9>
- Zhang HN, Chen CX, Zheng Y, Yu QQ, Zhang W (2020) Centrifuge modeling of layered rock slopes susceptible to block-flexure toppling failure. *Bull Eng Geol Environ* 79:3815–3831
- Zhao L, Wang J, An LL, Wang L, Xiang, Liang RY (2015) A case study integrating numerical simulation and GB-InSAR monitoring to analyze flexural toppling of an anti-dip slope in Fushun open pit. *Eng Geol* 197:20–32
- Zheng Y, Chen C, Liu T, Ren Z (2021) A new method of assessing the stability of anti-dip bedding rock slopes subjected to earthquake. *Bull Eng Geol Environ* 80:3693–3710
- Zheng Y, Chen CX, Liu TT, Song DR, Meng F (2019) Stability analysis of anti-dip bedding rock slopes locally reinforced by rock bolts. *Eng Geol* 251:228–240
- Zheng Y, Chen CX, Liu TT, Xia KZ, Liu XM (2017) Stability analysis of rock slopes against sliding or flexural-toppling failure. *Bull Eng Geol Environ* 77(4):1383–1403
- Zheng Y, Chen CX, Liu TT, Zhang HN, Xia KZ, Feng L (2018) Study on the mechanisms of flexural toppling failure in anti-inclined rock slopes using numerical and limit equilibrium models. *Eng Geo* 237:116–128
- Zheng Y, Chen CX, Meng F, Zhang HN, Xia KZ (2020a) Assessing the stability of rock slopes with respect to block-flexure toppling failure using a force-transfer model and genetic algorithm. *Rock Mech Rock Eng* 53:3433–3445
- Zheng Y, Chen CX, Meng F, Liu TT, Xia KZ (2020b) Assessing the stability of rock slopes with respect to flexural toppling failure using a limit equilibrium model and genetic algorithm. *Comput Geotech* 124:103619